

The role of alkylamine in the stabilization of CuO nanoparticles as a determinant of the Al/CuO redox reaction

Ségolène Palussière,^{a,b} Jérémy Cure,^b Andrea Nicollet,^a Pierre Fau,^b Katia Fajerweg,^b Myrtil L. Kahn,^b Alain Estève,^a Carole Rossi*^a

^a LAAS-CNRS, The University of Toulouse, 7 Avenue du colonel Roche, F-31400 Toulouse, France

^b LCC, The University of Toulouse, 205 Route de Narbonne, F-31400 Toulouse, France

Abstract

We report on a new strategy to synthesize Al/CuO nanothermites from commercial Al and ultra-small chemically synthesized CuO nanoparticles coated with alkylamine ligands. These usual ligands stabilize the CuO and prevent them from aggregation, with the goal to enhance the interfacial contact between Al and CuO particles. Using a variety of characterization techniques, including microscopy, spectroscopy, mass spectrometry and calorimetry (ATG/DSC), the structural and chemical evolution of CuO nanoparticles stabilized with alkylamine ligands are analyzed upon heating. This enables us to depict the main decomposition processes taking place at the CuO surface at low temperature (< 500 °C): the ligands fragment into organic species accompanied with H₂O and CO₂ release, which promotes the CuO reduction into Cu₂O and further Cu. We quantitatively discuss these chemical processes highlighting for the first time the crucial importance of synthesis conditions that control the chemical purity of the organic ligands (octylamine molecules and derivatives such as carbamate and ammonium ions) on the nanothermite performances. From these findings, an effective method to overcome the ligands-induced CuO degradation at low

temperature is proposed and Al/CuO nanothermite reaction is analyzed, in terms of onset temperature and energy released. We produce original structures composed of aluminium nanoparticles embedded in CuO grainy matrixes exhibiting onset temperature ~ 200 °C below usual Al/CuO onsets, having specific combustion profiles depending on synthesis conditions, while preserving the total amount of energy released.

1. Introduction

Nanothermites have received increasing interest over the two last decades because of their high volumetric energy densities (up to 16 kJ/cm^3), adiabatic flame temperature (> 2600 °C), and high reaction (burn) rates. They feature an exothermic redox reaction involving aluminum (Al) and a metal oxide, which results in a stable product after reaction. Different nanothermites with specific shapes (nanowires,¹⁻³ core-shell, ^{4,5} nanoparticles (NPs) mixture,⁶⁻¹³ nanofoils ¹⁴....), length scale (10 to few 100 nm), have been actively investigated for a wide range of applications including explosive additives, propellant rate modifiers,¹⁵ welding,¹⁶ and also for micro initiation and environmentally clean primers.¹⁷ Altogether, this research effort has experimentally demonstrated that a variety of different combustion effects can be obtained by manipulating the reactive system (Al and oxide) at the microscale, which cannot be achieved with bulk materials only. Typically, maximizing Al and oxidizer interfacial contact is paramount for achieving optimum reaction kinetics (combustion efficiency and ignitability), and numerous approaches have been reported in the literature to direct and optimize the nanoparticles assembly. ⁶ It can be done in inorganic, aqueous or organic solutions, using aerosols or sol-gel methods.¹⁸⁻²⁰ Kim *et al.* proposed a method in which the Al and Fe_2O_3 self-assembly is controlled by the electrostatic forces

which exist between charged aerosol particles.²¹ Another alternative is to use complementary DNA strands to control the structure of the nanothermites by guiding the self-assembly of the nanoparticles to enhance the energy release.^{22–24} A recent approach demonstrates that Al and oxide nanoparticles assembled on functionalized graphene sheets form highly reactive macrostructures.²⁵

In this work, a novel stabilizing strategy has been developed to synthesize Al/CuO nanothermites from Al and ultra-small CuO NPs functionalized with alkylamine ligands. These usual ligands stabilize the CuO NPs and prevent them from aggregation, which can be beneficial to enhance the coating of Al particles with smaller CuO NPs. Thus synthesized CuO NPs are then mixed in hexane with commercial Al NPs to form the nanothermite composite following an assembly process. The resulting nanothermites exhibit a weak Al+CuO redox reaction preceded by several low temperature exotherms that are investigated in the present study. The reduction of CuO NPs capped with alkylamine ligands into an intermediate Cu₂O phase is observed at ~250 °C before further reduction to metallic copper at ~450 °C *i.e.* prior to the thermite reaction onset. This contrasts with what is typically observed in bulk CuO in both isothermal and ramping reduction conditions, which requires high temperature to get reduced (527 and 877 °C for CuO → Cu₂O and Cu₂O → Cu, respectively). This work provides a detailed understanding of the early CuO reduction process due to the oxidation of the surrounding ligands before presenting an effective method to overcome it. After the chemical synthesis, the CuO are annealed at 500 °C (ramping 5 °C.min⁻¹) under oxygen atmosphere to eliminate organics and re-oxidize the reduced CuO. These annealed CuO nanoparticles mixed with commercial Al exhibit lower onset temperature compared to nanothermites produced from CuO commercial nanoparticles while releasing the same total energy.

2. Materials and methods

Chemicals and reagents

All chemicals products are ordered from Sigma Aldrich, excepted copper monochloride (Acros Organics). Commercial aluminum (Al, 99.9+%) and copper oxide (CuO, 99%) nanoparticles are supplied by US research nanomaterials (Texas, USA) and have an average particle size of 96 ± 43 nm and 31 ± 15 nm, respectively. The particles are largely spherical. The active Al mass ratio determined by thermogravimetric analysis (TGA) is 69 %.

*Synthesis of N,N'-diisopropylacetamidinate copper [Cu(*i*Pr-Me-AMD)]₂:*²⁶ A solution of methyllithium (1.6 M in Et₂O, 0.02 mol, 1 eq.) is added dropwise by syringe into a solution of 1,3-diisopropylcarbodiimide (0.02 mol) in 30 mL of Et₂O at -30°C. The solution is stirred for 4 h at room temperature. The resulting solution is then transferred to a copper monochloride (1.98 g, 0.02 mol) solution in 25 mL of dried Et₂O. The solution is stirred for 18 h under argon atmosphere. The solvent is removed under reduced pressure, and the resulting solid is extracted with dried pentane (75 mL). The pentane-extracted solid is filtered through a glass frit to afford a pale yellow solution. A saturated solution is formed by removing part of the pentane under reduced pressure. The powder is recrystallized in 5-10 mL of pentane and stored at 7 °C for 3 days. Colourless crystals [Cu(*i*Pr-Me-AMD)]₂ are obtained after removing the pentane under reduced pressure, and stored under inert atmosphere at 7 °C (30 %).

Synthesis of CuO nanoparticles by wet chemistry

Two batches of CuO NPs are produced following an organometallic route described previously from a N,N'-diisopropylacetamidinate copper precursor and

octylamine (OA) as a stabilizing agent. The reaction is complete after 16 h as confirmed by NMR analyses reported in a precedent work.²⁷ CuO NPs grown either by hydrolysis and/or oxidation in the ambient air (named CuO_air thereafter), or by oxidation under O₂ atmosphere (named CuO_O₂ thereafter). For CuO_air, the precursor [Cu(ⁱPr-Me-AMD)]₂ (0.24 mmol, 1 eq.) is mixed with octylamine (1.95 mmol, 8 eq.) under argon atmosphere, and then exposed to ambient air at room temperature. This leads to the reaction of OA with H₂O and CO₂ molecules, resulting in the formation of carbamate/ammonium species (RNCO₂⁻/RNH₃⁺). For CuO_O₂, the as prepared mixture [Cu(ⁱPr-Me-AMD)]₂ / OA contained in a flask, is placed into a reactor and purged by a O₂ line at 0.3 bar, giving a black/brown liquid after 1 h.

A summary of the materials used in this work is provided in **Table 1**.

Table 1. Database of Al and CuO nanoparticles used in the experiments:

Material	Source	Mean diameter (nm)
Al (purity 69 %)	US research nanomaterials	96 ± 43 nm (TEM)
CuO_com	US research nanomaterials	31 ± 15 nm (TEM)
CuO_air	US research nanomaterials	6.8 ± 2.2 nm (TEM)
CuO_O ₂	US research nanomaterials	3.8 ± 0.7 nm (TEM)

Preparation of Al/CuO nanothermites

To prepare the nanothermites, chemically synthesized CuO NPs (CuO_air and CuO_O₂) are first washed by centrifugation (8700 rpm, room temperature, 10 min) with ethanol and acetone in order to remove excess of ligands that are not coordinated onto the nanoparticles surface. The mass losses for CuO_air and CuO_O₂ correspond to 72 and 87 % of their initial mass, respectively. Then, they are mixed with commercial Al nanoparticles following the procedure depicted in Figure 1. Three batches of Al rich nanothermites (Al to CuO mass ratio of 1.2) are then prepared, which are named

Al/CuO_{air}, Al/CuO_{O₂} and Al/CuO_{com} thereafter. Al/CuO_{com} constitutes the reference system. All nanothermite mixtures are sonicated in a hexane suspension for a total of 10 min in an ultra-sonic bath before being dried at 70 °C under vacuum.

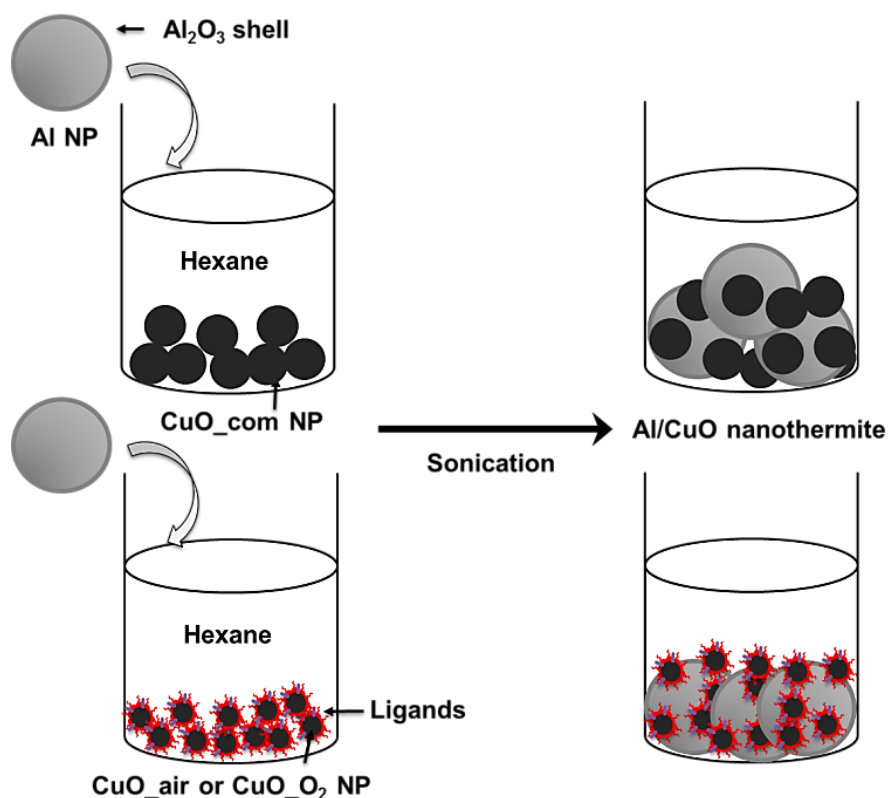


Figure 1. Schematic of the synthesis of CuO nanoparticles following an organometallic route, in the ambient air and under O₂ atmosphere of the experimental protocol used to prepare Al/CuO nanothermites.

Functionalization of commercial CuO NPs (CuO_{com})

To check the reduction effects of AO ligands on CuO_{com}, a batch of CuO_{com} nanoparticles (500 mg, 6.29 mmol) are functionalized with OA (18.3 mg, 0.14 mmol) by mixing them and stirred for 1 h in the ambient air. The mixture is centrifuged (8700

rpm, RT, 10 min) and CuO_com@OA nanoparticles are retrieved before chemical and thermal analysis.

Characterization of CuO and Al NPs

The morphology, particle size, agglomeration are observed by TEM (Transmission Electron Microscopy) using a JEOL JSM operating at 100 kV. Analyses of the images are performed using ImageJ. The thermal decomposition of CuO NPs are characterized under a ramping heating profile @ 10 °C.min⁻¹ by Thermogravimetric/Differential Scanning Calorimetry (TGA/DSC) using a Mettler Toledo Thermogravimetric analyzer. Experiments are performed with ~5 mg of CuO nanopowders in platinum crucibles over a temperature ranging from ambient to 500 °C.

The chemical composition of the materials is characterized using a SEIFERT XRD 3000 TT X-Ray Diffractometer (XRD) with Cu-K α radiation ($\lambda = 1.54059 \text{ \AA}$) fitted with a diffracted-beam graphite monochromator. The diffraction angle (2θ) is scanned from 10 to 80°. The decomposition of CuO particles is investigated using MS (mass spectroscopy) (Pfeiffer Omnistar 1-200 uma), with temperature range from ambient temperature to 500 °C with a heating rate at 10 °C.min⁻¹. All measurements are performed under Ar flowing gas (99.999%).

Characterization of nanothermites Al/CuO

The thermal properties of nanothermites are characterized by DSC using a NETZSCH DSC 404 F3 pegasus device equipped with a DSC-C_p sensor type S. ~5 mg of

nanothermites are analyzed in a platinum crucible over a temperature ranging from ambient to 1000 °C with a heating rate of 10 °C· min⁻¹.

Additionally, a SEM (Scanning Electron Microscopy) Helios 600i instrument coupled with an EDX (Energy Dispersive X-ray spectrometry) spectroscopy system to conduct elementary analysis is used to image nanothermites. For the observations, samples are prepared by depositing and evaporating one droplet of the nanoparticles solution onto a silicon wafer.

3. Results and discussion

Chemical and structural characterization of CuO and Al NPs

Representative TEM images of the synthesized CuO NPs (CuO_{air} and CuO_{O₂}), CuO_{com} and Al NPs are shown in Figure 2, with the addition of size distribution following a Gaussian fit. The CuO_{air} objects are characterized as polymorphous shapes and mean diameter of 6.8 ± 2.2 nm, whereas CuO_{O₂} particles exhibit smaller size with a mean diameter of 3.8 ± 0.7 nm and more isotropic morphologies. On the contrary, CuO_{com} displays large particles with an extended size distribution from 15 to 120 nm and mean diameter of 31 ± 15 nm. In the same way, Al NPs feature spherical shapes with a mean diameter of 96 ± 43 nm. The synthesis of CuO NPs allows an exquisite control on getting smaller size and monodispersity down to the nanoscale, due to the slow and homogeneous chemical interplay between ligands (OA and/or carbamate) and growing CuO particles.²⁷

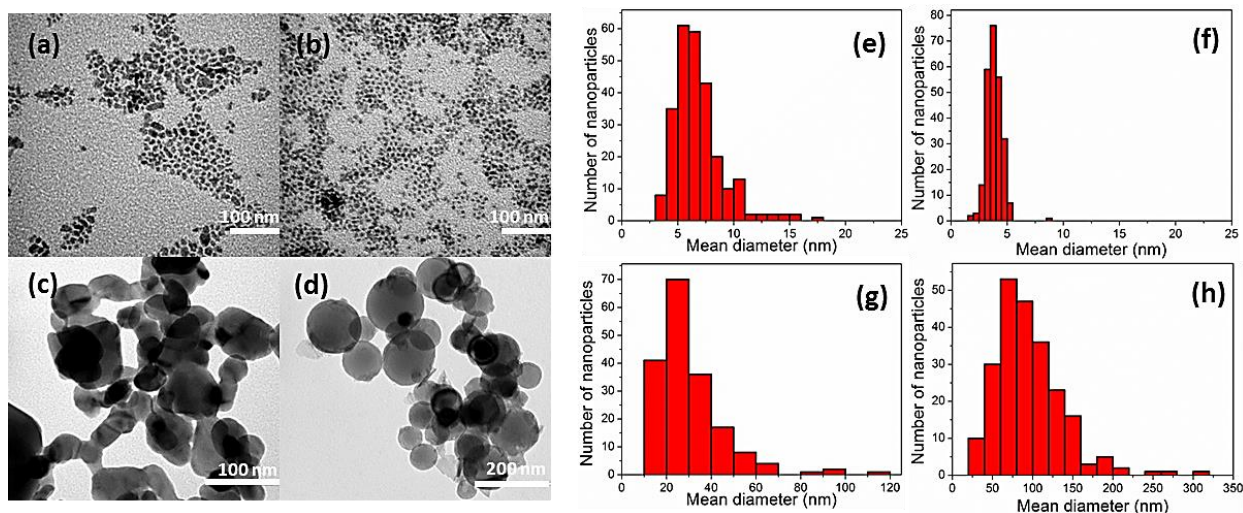


Figure 2. TEM images of (a) CuO_{air}, (b) CuO_{O₂}, (c) CuO_{com} (d) and Al NPs. The mean diameter is evaluated by fitting of the histogram with a Gaussian curve, extracted from TEM micrographs of 250 particles for (e) CuO_{air}, (f) CuO_{O₂}, (g) CuO_{com}, (h) Al NPs.

Figure 3 shows XRD diagrams corresponding to CuO_{air}, CuO_{O₂} and compared with CuO_{com}. Overall, CuO_{air} and CuO_{O₂} NPs exhibit similar patterns in the 30° to 80° region, which corresponds to the monoclinic symmetry (space group C2/c) of the CuO tenorite structure, the (111) stable surface being dominant. However, synthesized CuO NPs show broader peaks compared to CuO_{com}. Applying the Debye-Scherrer formula to the diffraction measurements gives the crystallite size that compose the NP's structure.²⁸ CuO_{air} and CuO_{O₂} have crystallite sizes of 6.7 ± 1.0 and 4.4 ± 0.5 respectively, indicating that they can both be considered as single nanocrystals whereas CuO_{com} NPs exhibit much broader disparity and crystallite sizes that may indicate a multi-grain composition.

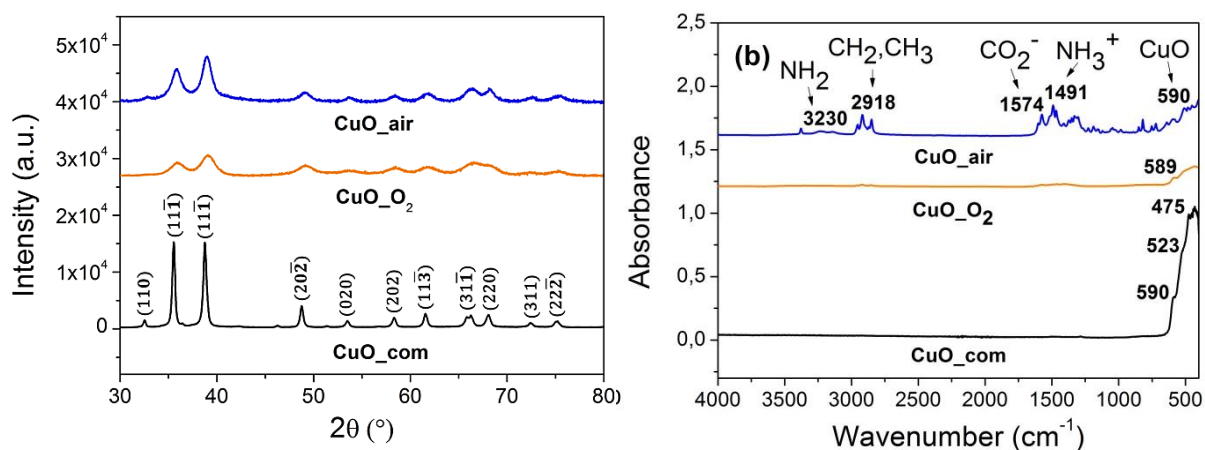


Figure 3. X-ray diffraction patterns (a) and FTIR spectra (b) obtained on CuO_{air}, CuO_{O₂} samples being washed and compared with CuO_{com}.

To further investigate the interactions between CuO particle surfaces and ligands, ATR-FTIR absorbance spectroscopy is performed and results are shown in Figure 3b. The stretching modes of the CuO bonds in CuO_{com} are clearly detected at low wavenumbers, 590 cm⁻¹, 523 cm⁻¹ and 475 cm⁻¹. However, as for XRD analyses, some differences are found between synthesized CuO NPs in air and controlled O₂ atmosphere. The low intensity of signal between 3000 and 700 cm⁻¹ obtained for CuO_{O₂} is clearly explained by the fact that only a small quantity of ligands remains absorbed on CuO surface after washing. Nevertheless, a weak peak can be detected around ~2918 cm⁻¹ corresponding to C-H vibrational modes, which confirms the presence of ligands around CuO particles.

Focusing on CuO_{air}, in addition to C-H modes from the alkyl groups (CH₂) at 2953, 2918 and 2851 cm⁻¹, characteristic peaks at 3379, 3320, 3141 cm⁻¹ and 1574 cm⁻¹ are associated to N-H and N-H₂ and C-O₂ modes. Those bands are characteristic to the carbamate/ammonium species (R-NH₃⁺ + R-NHCO₂⁻), formed when OA is exposed to carbon dioxide and water present in ambient air. Supported by Bacsik *et al.*³³ who

investigate properly the band positions of chemical functions of the carbamates ions pairs via IR spectroscopy, by heating and looking at the desorption of carbon dioxide, we conclude that specific peaks between 1600 and 700 cm^{-1} are attributed to the ammonium and carboxylate groups of the ammonium carbamate species at different stretching symmetry. This reaction does not occur in the case of CuO_2 synthesis, i.e. where the atmosphere does not contain neither carbon dioxide nor water molecules. These ion pairs may bind to CuO nanoparticles with a higher stabilization than neutral amine terminations being largely eliminated through washing, thus playing a dominant role in the ligand shell stabilization. ³²

In summary, although in both synthesis routes, ligands include OA and amidine resulting from the decomposition of the copper (I) acetamidinate precursor, they react differently with the CuO surface depending on the environmental atmosphere.

Thermal properties of Al/CuO nanothermites

The sonication of the Al and CuO NPs in hexane leads to homogeneous mixtures that are observed in the TEM photographs (Figure 4). The Al/CuO_{com} mixtures (Figure 4a) contain aggregates with spread homogeneous mixture of spherical Al and CuO NPs. Furthermore, Al/CuO_{air} mixtures (Figure 4b) show a heterogeneous distribution unlike Al/CuO_{O₂} ones (Figure 4c) where small CuO NPs cover Al NPs, pointing to the intimate interfacial contact between Al and CuO NPs. Therefore the amount of small CuO NPs around Al NPs is greater than for the Al/CuO_{com} mixture.

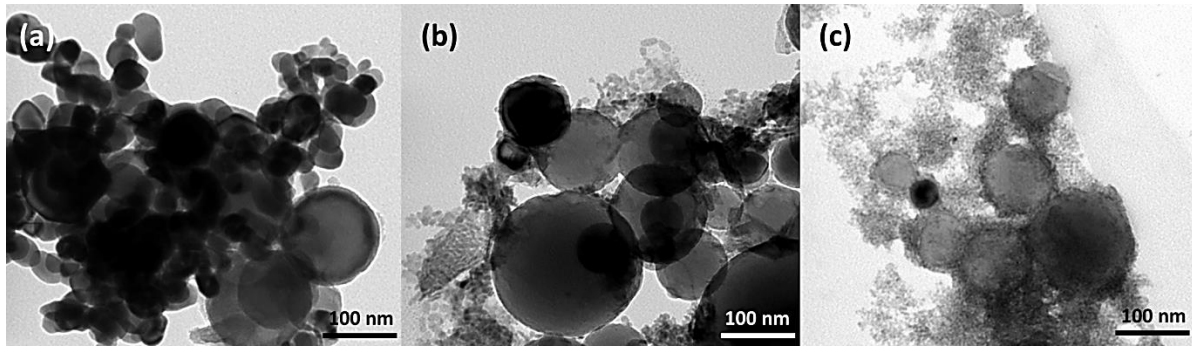


Figure 4. TEM images of the different Al/CuO mixtures prepared following the experimental protocol depicted in the Figure 1 from commercial Al NPs mixed with (a) CuO_com, (b) CuO_air and (c) CuO_O₂.

The results of DSC experiments are presented in Figure 5. Al/CuO_com (Figure 5a) exhibits two major exothermic peaks and one endotherm after 500 °C, whereas Al/CuO_air and Al/CuO_O₂ (Figure 5b and c) show weaker exothermic peaks at similar temperatures, typically associated with the thermite reaction between CuO and Al nanoparticles.¹⁷ The temperatures associated with these exothermic and endothermic reactions, as well as the heat released between 450 and 900 °C are summarized in Table 2. Following the first exothermic peak **(i)** at 578 °C, which corresponds to the reaction of solid Al with CuO, the small endotherm **(k)** is attributed to the melting of Al at 658 °C. A second exothermic peak **(j)**, caused by the reaction of liquid Al with solid Cu₂O and some CuO, occurs at 783 °C. During this reaction, the amorphous alumina transforms into γ Al₂O₃,²⁹ which explains the sharp decrease in the DSC. However, we still can identify and interpret some thermal responses on the DSC curves of Al/CuO_air and Al/CuO_O₂. The most significant one is the intense endotherm seen in the Al/CuO_air system at 189 °C that is not detectable in the Al/CuO_O₂ system. In addition, two exotherms are observed slightly above 200 °C and the heat released between 450 and 900 °C for Al/CuO_O₂ is higher than that for

Al/CuO_{air} (see Table 2). To summarize, we clearly observe three different thermal responses depending on the CuO NPs used, highlighting the role of synthesis protocol and ligands nature in the hindering of the thermite reaction.

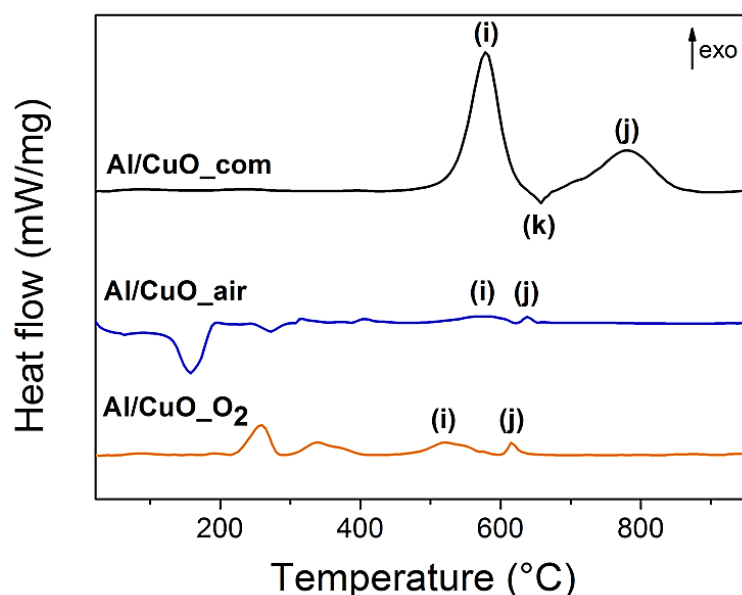


Figure 5. DSC curves obtained for (a) Al/CuO_{com}, (b) Al/CuO_{air} and (c) Al/CuO_{O₂}. Indexed peaks are described in Table 2.

Table 2. Detail of reactions associated to the thermal responses of nanothermites plotted in Figure 5.

Indexed peaks	Temperature Al/CuO _{com} (°C)	Temperature Al/CuO _{air} (°C)	Temperature Al/CuO _{O₂} (°C)	Reactions associated
(i)	578	558-588	520	Al + O
(j)	658	638	615	Al melting
(k)	783	/	/	Al + O
Heat released (450-900 °C) (kJ.g ⁻¹)	0.95	0.24	0.50	

Understanding the interaction of ligands with CuO hindering the Al/CuO redox reaction

To get into further details on the reaction of CuO nanoparticles with their surrounding chemical cues, neat CuO_{air} and CuO_{O₂} NPs are chemically analyzed upon ramping from ambient to 500 °C. TGA curves (Figure 6a) show that commercial powders, CuO_{com}, feature no mass loss whereas CuO_{air} and CuO_{O₂} lose a total of 58 % and 29 % of their initial mass, respectively. For both synthesized CuO NPs, the mass loss occurs in three consecutive steps. The first one occurs at ~200 °C and the mass loss is much pronounced for CuO_{air} (~37 %) compared to CuO_{O₂} (~ 4 %). The two other loss steps (at 285 °C and 412 °C, respectively) show similar behaviour for both sets of NPs. In parallel to TGA, DSC measurements are also recorded for the three batches of CuO NPs (see Figure 6b): while no peak is observed for CuO_{com} in the range of ambient - 500 °C, both synthesized CuO NPs exhibit different reactions and associated thermal signatures at temperatures lower than the expected Al-O reactions. Results are consistent with DSC traces presented earlier (Figure 4b and c). The main difference between both sets of NPs concerns the CuO_{air} endotherm peak, noted **(l)**, which is followed by two exotherms **(m)** and **(n)** also visible for CuO_{O₂}, while being less intense.

Whatever the synthesized CuO conditions, the significant mass loss asserts that decomposition reactions are taking place at the CuO particle surface.

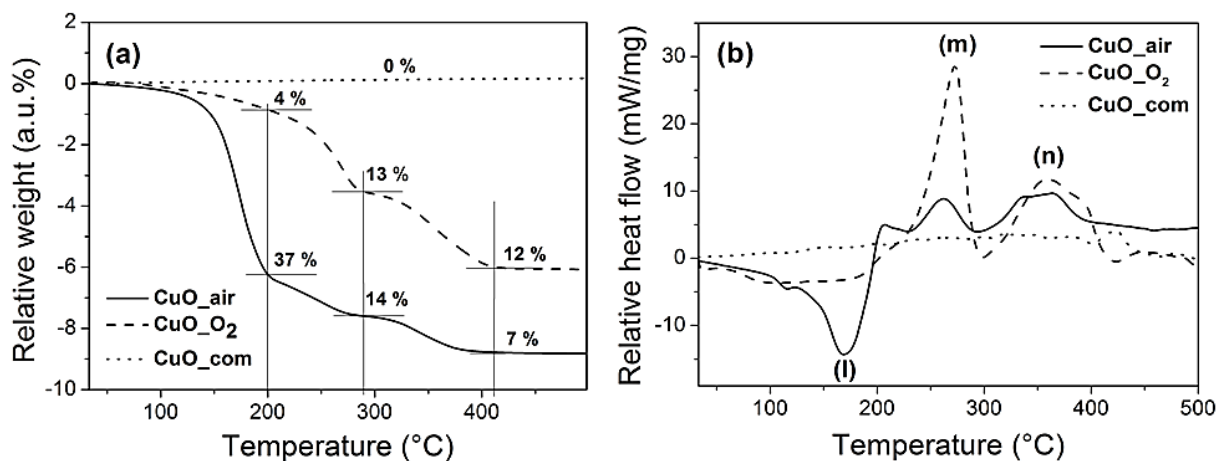


Figure 6. (a) TGA and (b) DSC curves of CuO_{air}, CuO_{O₂} and CuO_{com} NPs under Ar atmosphere and ramping of 10°C.min⁻¹.

Mass spectrometry analyses of both synthesized CuO NPs upon heating (@ 10°C.min⁻¹) under argon atmosphere reveal that mass losses are accompanied with the release of different species. Figure 7 shows MS spectra for both CuO_{air} and CuO_{O₂} at ambient temperature (AT), 100, 175, 235, 280, 341, 382 and 400 °C. A typical commercial CuO background spectrum for the mass spectrometer consists of a large peak at mass to charge ratio (m/z) 18 (H₂O), smaller peaks at m/z 28 (N₂) and m/z 32 (O₂).³⁰ Detailed mass spectra, included all detected m/z species, during the CuO_{air} and CuO_{O₂} ramping are given in supplementary file, Figure S1 and Table S1.

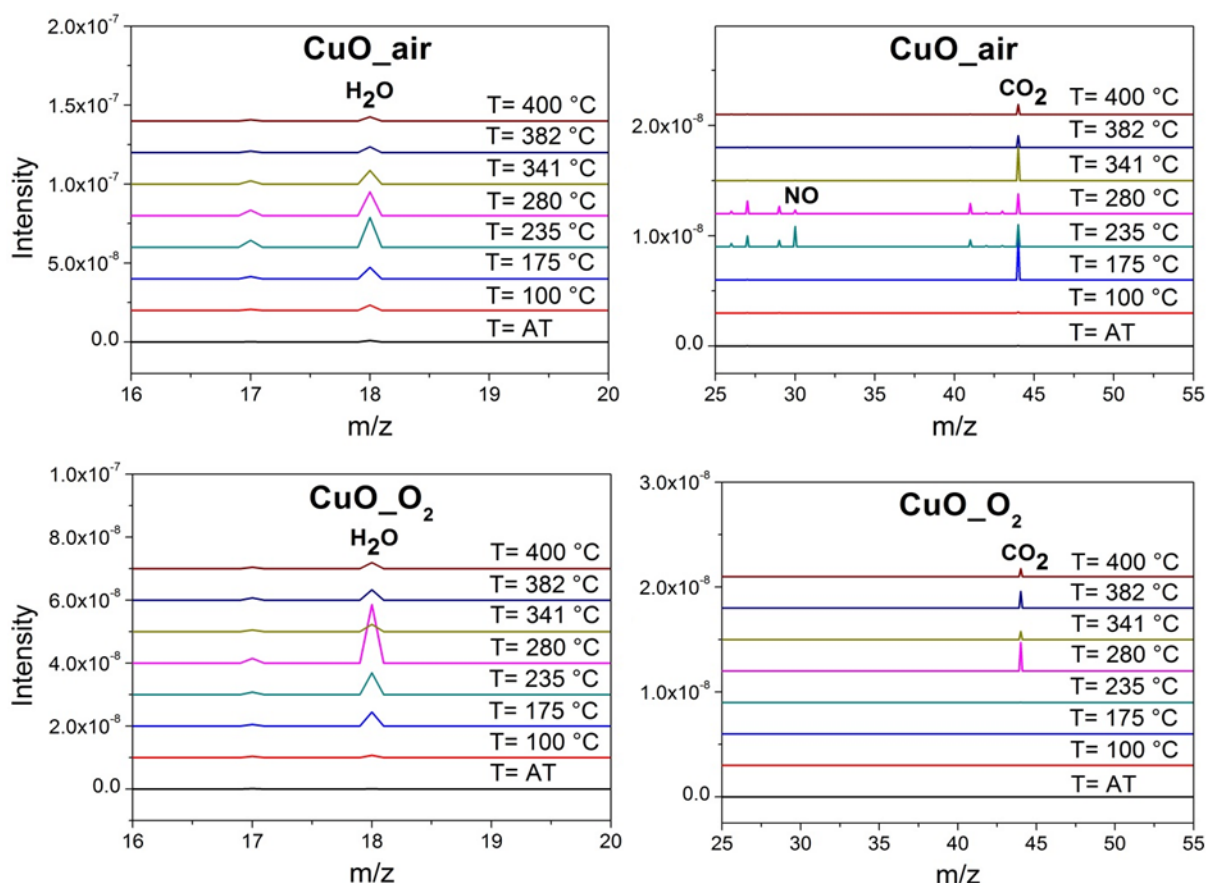


Figure 7. MS responses of (a) CuO_{air} and (b) CuO_{O₂} plotted at various temperatures under Ar atmosphere, zoomed around m/z 18 (H₂O), m/z 30 (NO) and m/z 44 (CO₂). Ramping is 10°C.min⁻¹. AT: ambient temperature.

For both CuO_{air} and CuO_{O₂}, the major decomposition products include m/z 18 (H₂O) and m/z 44 (CO₂). These observations can be better understood by quantifying the kinetics of desorption plotted in supplementary file (Figure S2). Importantly, H₂O molecules start to be released at room temperature for CuO_{air} and in larger amounts compared to CuO_{O₂}, whereas the kinetics of H₂O molecules release is similar for both CuO (see Figure S2). This is consistent and matches well the endotherm peak **(I)** seen in DSC analyses (Figure 6b). This is also consistent with the chemical nature of CuO NPs grown under air, where OA ligands are potentially decomposed into

carbamate/ammonium ion pairs ($\text{RNCO}_2^-/\text{RNH}_3^+$) due to the reaction with ambient H_2O and CO_2 , as suggested also from FTIR results (Figure 3b). In such a scenario, these ions should increase the polarity of the surface, facilitating the adsorption of water molecules, despite the presence of hydrophobic alkyl chains. On the contrary, the CuO_2 NPs exhibit less affinity with water molecules, indicating that the hydrophobic contribution of alkyl chains dominates. The wider range of temperatures in which water molecules are desorbed in CuO_{air} (see Figure S2) is another illustration of its surface/ligands chemical complexity, characterized by different adsorption configurations associated with the presence of ligands of different nature and organization (OA, carbamate, ammonium ...).

At 175 °C, CO_2 start to be released abruptly in CuO_{air} system which is earlier than what is observed for CuO_2 (280 °C). Increasing temperature up to 235 and 280 °C, NO species (m/z 30) are detected in CuO_{air} , which indicates that CuO_{air} are surrounded by more ligands and chemical species than CuO_2 .

To summarize MS experiments, upon ramping heating, the ligands decomposed into fragments (H_2O , R-CO_2 , R-NH_3 ...) with a release of CO_2 and H_2O occurring at ~270-280 °C for both CuO NP systems. The exothermic peaks **(m)** and **(n)** in Figure 6b can therefore be attributed to the oxidation of some released species (R-CO_2 , R-NH_3 ...) with oxygen from the CuO surface. XRD diagrams (Figure 8) of CuO_{air} (a) and CuO_2 (b) taken at 200 and 500 °C clearly show the CuO_{air} decomposition into cuprite (Cu_2O , major phase) at 200 °C and, to a lesser extent, copper. At 200 °C, the decomposition of CuO_2 is less pronounced, as cuprite phase is present but still represents a minor phase. At 500 °C, for both samples, copper structure is the main phase with the presence of a small quantity of Cu_2O . Early reduction of CuO is confirmed by FTIR analysis given in supporting information, Figure S3: cuprite phonon

modes at 616 cm^{-1} is evidenced at $200\text{ }^{\circ}\text{C}$ for both samples, whereas they disappear at $500\text{ }^{\circ}\text{C}$ when copper is formed. These effects are even stronger for CuO_air with the formation of copper at $200\text{ }^{\circ}\text{C}$, due to the larger quantity of ligands and water at the CuO surface. XRD analysis of CuO_com annealed at 200 and $500\text{ }^{\circ}\text{C}$ under argon is presented in Figure S4. The initial CuO structure doesn't change until $500\text{ }^{\circ}\text{C}$, pointing to the crucial role of the ligands in the CuO reduction process below $500\text{ }^{\circ}\text{C}$ observed for CuO_air and CuO_O₂.

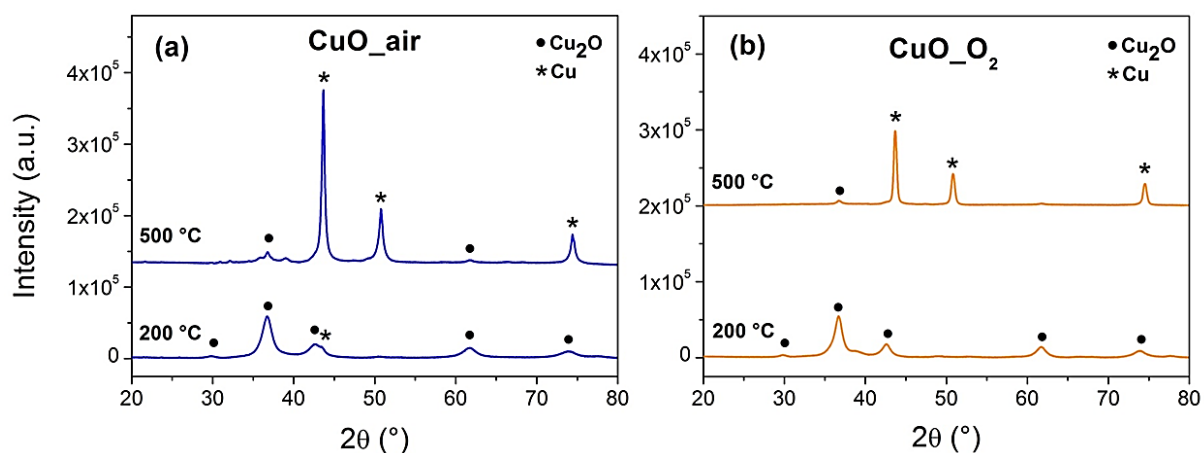


Figure 8. X-ray diffraction patterns of (a) CuO_air and (b) CuO_O₂ taken at 200 and $500\text{ }^{\circ}\text{C}$ upon annealing with a ramping of $5\text{ }^{\circ}\text{C}\cdot\text{min}^{-1}$ and under argon.

The early reduction of CuO in the case of ultra-small particles has been evidenced by Pike *et al.* who observed the reduction of CuO nanoparticles being $4\text{--}16\text{ nm}$ in width at $250\text{ }^{\circ}\text{C}$ using a ramping heating profile, in CO₂ atmosphere.³¹ Altogether these results also question on the effect of CuO nanoparticles size on their stability in temperature, i.e. ability to withstand a higher temperature before their reduction into Cu₂O and then to metallic copper nanoparticles. To address this question, larger particles, CuO_com, are functionalized with OA (named CuO_com@OA) and

characterized upon ramping at $10^{\circ}\text{C}\cdot\text{min}^{-1}$ in Ar atmosphere (See supporting information S5). Figure S5 displays FTIR and XRD characterization of CuO_com@OA showing alkyl chain of OA at the stretching mode in the area of 3000 cm^{-1} , proving that bonding is realized between OA and commercial CuO. XRD analysis of annealed CuO_com@OA (Figure 5b) demonstrates that at 500°C , CuO phase is partially reduced into Cu_2O and Cu phases. The DSC diagram of CuO_com@OA mixed with Al (Figure S5c) exhibits a heat release of $0.79\text{ kJ}\cdot\text{g}^{-1}$ between 450 and 900°C . Altogether, this confirms the role of ligands in the reduction process of CuO nanoparticles but also that, in the case of bigger particles, CuO phase is still present after 500°C , allowing the reaction with Al. Therefore, CuO nanoparticles size has to be taken into account with precision to avoid early reduction.

Optimization process: atmosphere controlled thermal treatment of CuO nanoparticles

To overcome the early reduction of ultra-small CuO nanoparticles, the synthesized CuO nanoparticles are annealed at 500°C under oxidizing environment to burn the organic coating without reducing the CuO and enhance their size. In Figure 9, XRD diagrams show CuO_air and CuO_O₂ annealed under oxygen at 200 and 500°C . Surprisingly, at 200°C , CuO_air reduces mainly into copper and Cu_2O whereas CuO_O₂ partly remains as CuO structure, but with a strong reduction component into Cu_2O . The CuO reduction process appears inevitable due to the preference of ligands to extract oxygen atoms from the CuO surface instead of reacting with oxygen molecules from the atmosphere. Since ligands are coordinated to the surface, oxygens from CuO surface are more available for the oxidation compared to those in the atmosphere. However, at 500°C both CuO_air and CuO_O₂ get re-oxidized into a tenorite structure with a remaining minor cuprite phase for the CuO_air system.

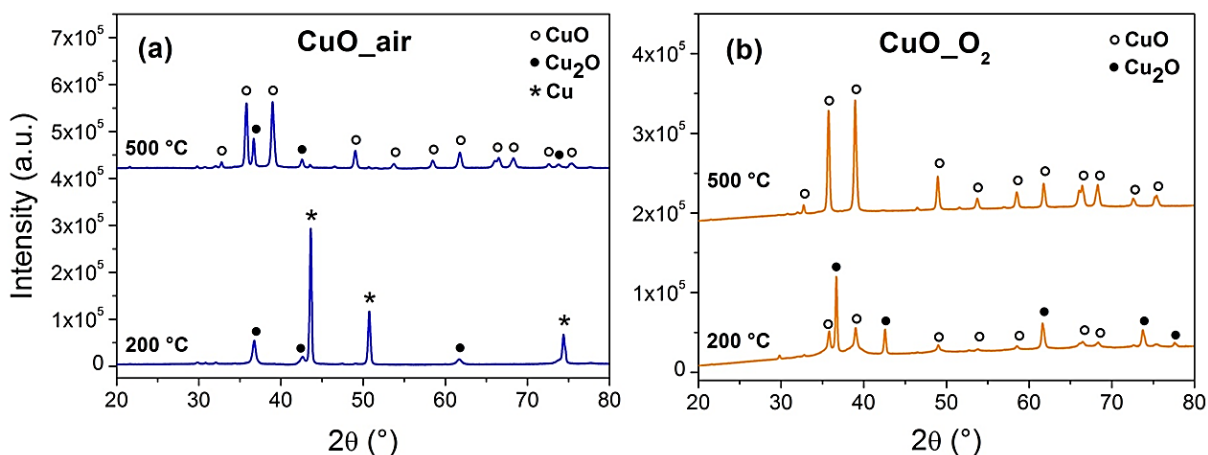


Figure 9. X-ray diffraction patterns of (a) CuO _air and (b) CuO_O₂ taken at 200 and 500°C upon annealing with a ramping of 5°C.min⁻¹ and under oxygen.

Annealed CuO nanoparticles grow during the heating treatment that could be the effect of nanoparticles sintering. From XRD spectra (Figure 9), crystallite size is evaluated at 33 ± 6 nm and 41 ± 8 nm for annealed CuO_air and CuO_O₂, respectively.

After mixing with Al commercial NPs, SEM pictures in Figure 10, show large aggregates in which some spherical commercial Al NPs are embedded into CuO (Figure 10a and see chemical analysis by EDS provided in supporting information Figure S6). CuO are organized as extended domains of sintered particles, as shown in Figure 10c. Figure 10d exhibits homogenous repartition of Al NPs around the CuO_O₂ aggregates.

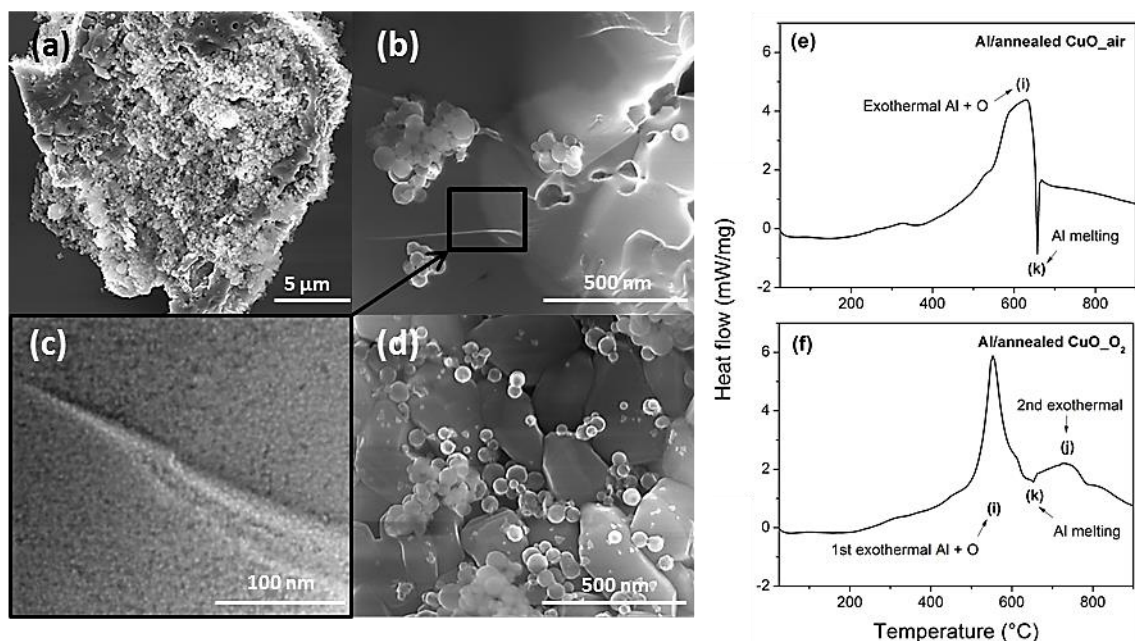


Figure 10. SEM images of (a) and (b) Al/annealed CuO_{air} mixtures, (c) zoom on annealed CuO_{air} particles in the CuO_{air} aggregate and (d) Al/annealed CuO_{O₂}. DSC curves of (e) Al/annealed CuO_{air} nanothermites and (f) Al/annealed CuO_{O₂} nanothermites. Indexed peaks are described in Table 3.

Finally, the thermal performances of both nanothermites obtained by mixing Al NPs with annealed CuO NPs are characterized by DSC and diagrams are given in Figure 10. Two exotherms (**i** and **j**) are observed for the Al/annealed CuO_{O₂} mixture (Figure 10e) whereas only one (**i**) is present for the Al/annealed CuO_{air} mixture (Figure 10f). For both nanothermites, the reaction onset occurs earlier than for the Al/CuO_{com} nanothermite (Figure 5). A strong endotherm appears at 650 °C (**k**) for Al/annealed CuO_{air} mixture (a) attributed to Al-Cu eutectic. The first and second exothermic peaks (**i** and **j**) are associated to the redox reaction. The total heat released for both nanothermites presented in Table 3 remains competitive with Al/CuO_{com} (Table 2). Importantly a major part of this total energy is released prior Al melting: 63 % and 48

% for Al/CuO_{air} and Al/CuO_{O₂} compared to 33% for Al/CuO_{com}. This is an interesting result for application requiring low temperature reactive materials.

Table 3. Thermal reactions associated to the Al/CuO mixtures in the Figure 10

Indexed peaks	Peak temperature Al/annealed CuO _{air} (°C)	Peak temperature Al/annealed CuO _{O₂} (°C)	Reactions associated
(i)	627	553	Al + O
(j)	657	653	Al ₂ Cu melting ; Al melting
(k)	/	725	Al + O
Heat released (kJ.g⁻¹) (450-900 °C)	0.81	0.93	

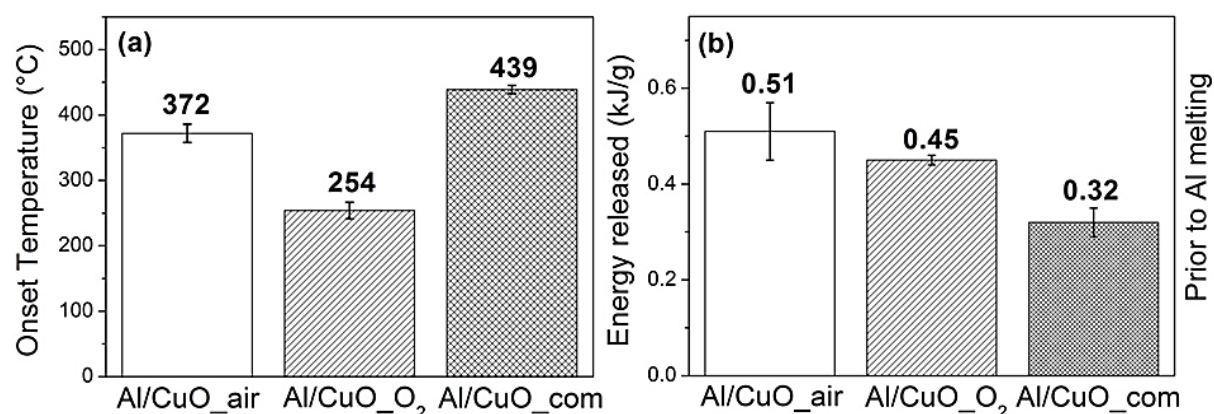


Figure 11. (a) Onset temperatures and (b) energy released prior 500 °C (b) determined from DSC curves of Al/annealed CuO_{air}, Al/annealed CuO_{O₂} (Figure 10a,b) and Al/CuO_{com} (Figure 5a) (Al:O ratio is 1.2).The energy released is calculated by integrating the first exotherm in the range of onset temperature - 500 °C. Error bars are calculated from the number of experiments done for the same conditions of preparation.

Conclusion

Copper oxide nanoparticles of 6 nm in average size were synthesized following an original organometallic route before being mixed with Al nanoparticles to form a nanothermite composite. As synthesized, we found that ligands coordinate to CuO nanoparticles leading to their early reduction that is significantly different from that of usual bulk CuO used in nanothermite composite. Notably the synthesized nanoparticle reduce to an intermediate Cu₂O phase at ~250°C before further reduction to metallic copper at ~450 °C. Thus, energetic performances of the nanothermites prepared from synthesized CuO show unexpected exothermic reactions below 500 °C. Using a variety of characterization techniques, including microscopy, spectroscopy, mass spectrometry and calorimetry, the structural and chemical evolution of CuO nanoparticles stabilized with ligands (alkylamine) were analyzed upon heating enabling us to unravel that, at low temperature (~200 °C), ligands fragment into organic species accompanied with important release of H₂O and CO₂ molecules. This process promotes the CuO reduction into Cu₂O and further Cu. Finally, we proposed an effective method to overcome the CuO degradation. After the synthesis, the CuO nanoparticles coated with the ligands are annealed in oxidizing atmosphere enabling the oxidation of ligands with the CuO reduction at low temperature, to finally re-oxidize the reduced CuO. The CuO nanoparticles increase in size while keeping roughly the same shape, probably being a matrix of sintered nanoparticles. Finally the thermites produced by mixing thus CuO particles with commercial Al ones exhibit earlier onset temperature than those produced from commercial CuO nanoparticles with similar heat of reaction.

Competting financial interests

The authors declare no competing financial interests.

Corresponding author

Correspondance to: Carole Rossi, rossi@laas.fr

Acknowledgements

We would like to thank Dr. Pierre Alphonse, Dr. Laure Vendier and Jean-François Meunier for their assistance and expertise in the TGA/DSC measurements, Xray diffraction analyses and mass spectroscopy measurements respectively. We also thank Severine Vivies for her collaboration in producing the nanothermites and their characterization. We thank the European Commission and Region Occitanie for their FEDER support (THERMIE grant) having funded the DSC equipment. We also thank the European Research Council as well as the university Fédérale de Toulouse for its financial support through the PyroSafe project (grant number 832889) and “chaire d’attractivité” MUSE, respectively.

References

- 1 K. Zhang, C. Rossi, C. Tenailleau and V. Conédéra, *Journal of Nanoscience and Nanotechnology*, 2009, **9**, 1418–1422.
- 2 K. Zhang, C. Rossi, C. Tenailleau, P. Alphonse and J.-Y. Chane-Ching, *Nanotechnology*, 2007, **18**, 275607.
- 3 Y. Yang, P. Wang, Z. Zhang, H. Liu, J. Zhang, J. Zhuang and X. Wang, *Scientific Reports*, 2013, **3**, 1694.
- 4 G.-Q. Zheng, W.-C. Zhang, X. Xu, R.-Q. Shen, J.-P. Deng and Y.-H. Ye, *Journal of Inorganic Materials*, 2015, **30**, 610–614.
- 5 Y. Ohkura, S.-Y. Liu, P. M. Rao and X. Zheng, *Proceedings of the Combustion Institute*, 2011, **33**, 1909–1915.
- 6 F. Séverac, P. Alphonse, A. Estève, A. Bancaud and C. Rossi, *Advanced Functional Materials*, 2012, **22**, 323–329.
- 7 D. S. Moore, S. F. Son and B. W. Asay, *Propellants, Explosives, Pyrotechnics*, 2004, **29**, 106–111.
- 8 M. R. Weismiller, J. Y. Malchi, J. G. Lee, R. A. Yetter and T. J. Foley, *Proceedings of the Combustion Institute*, 2011, **33**, 1989–1996.
- 9 A. Rai, L. Zhou, A. Prakash, A. McCormick and M. R. Zachariah, *MRS Online Proceedings Library Archive*.

- 10 S. Apperson, R. V. Shende, S. Subramanian, D. Tappmeyer, S. Gangopadhyay, Z. Chen, K. Gangopadhyay, P. Redner, S. Nicholich and D. Kapoor, *Appl. Phys. Lett.*, 2007, **91**, 243109.
- 11 B. S. Bockmon, M. L. Pantoya, S. F. Son, B. W. Asay and J. T. Mang, *Journal of Applied Physics*, 2005, **98**, 064903.
- 12 V. I. Levitas, B. W. Asay, S. F. Son and M. Pantoya, *Appl. Phys. Lett.*, 2006, **89**, 071909.
- 13 V. E. Sanders, B. W. Asay, T. J. Foley, B. C. Tappan, A. N. Pacheco and S. F. Son, *Journal of Propulsion and Power*, 2007, **23**, 707–714.
- 14 D. P. Adams, *Thin Solid Films*, 2015, **576**, 98–128.
- 15 D. G. Piercey and T. M. Klapötke, *Central European Journal of Energetic Materials*, 2010, **7**, 115–129.
- 16 A. J. Swiston, E. Besnoin, A. Duckham, O. M. Knio, T. P. Weihs and T. C. Hufnagel, *Acta Materialia*, 2005, **53**, 3713–3719.
- 17 L. Glavier, G. Taton, J.-M. Ducéré, V. Baijot, S. Pinon, T. Calais, A. Estève, M. Djafari Rouhani and C. Rossi, *Combustion and Flame*, 2015, **162**, 1813–1820.
- 18 J. Y. Malchi, T. J. Foley and R. A. Yetter, *ACS Appl. Mater. Interfaces*, 2009, **1**, 2420–2423.
- 19 R. Shende, S. Subramanian, S. Hasan, S. Apperson, R. Thiruvengadathan, K. Gangopadhyay, S. Gangopadhyay, P. Redner, D. Kapoor, S. Nicolich and W. Balas, *Propellants, Explosives, Pyrotechnics*, 2008, **33**, 122–130.
- 20 T. M. Tillotson, A. E. Gash, R. L. Simpson, L. W. Hrubesh, J. H. Satcher and J. F. Poco, *Journal of Non-Crystalline Solids*, 2001, **285**, 338–345.
- 21 S. H. Kim and M. R. Zachariah, *Advanced Materials*, 2004, **16**, 1821–1825.
- 22 T. Calais, V. Baijot, M. Djafari Rouhani, D. Gauchard, Y. J. Chabal, C. Rossi and A. Estève, *Langmuir*, 2016, **32**, 9676–9686.
- 23 T. Calais, D. Bourrier, A. Bancaud, Y. Chabal, A. Estève and C. Rossi, *Langmuir*, 2017, **33**, 12193–12203.
- 24 T. Calais, A. Bancaud, A. Estève and C. Rossi, *ACS Appl. Nano Mater.*, 2018, **1**, 4716–4725.
- 25 R. Thiruvengadathan, S. W. Chung, S. Basuray, B. Balasubramanian, C. S. Staley, K. Gangopadhyay and S. Gangopadhyay, *Langmuir*, 2014, **30**, 6556–6564.
- 26 Z. Li, S. T. Barry and R. G. Gordon, *Inorg. Chem.*, 2005, **44**, 1728–1735.
- 27 J. Jońca, A. Ryzhikov, S. Palussière, J. Esvan, K. Fajerweg, P. Menini, M. L. Kahn and P. Fau, *ChemPhysChem*, 2017, **18**, 2658–2665.
- 28 A. Guinier, *X-ray Diffraction in Crystals, Imperfect Crystals, and Amorphous Bodies*, Courier Corporation, 1994.
- 29 I. Abdallah, J. Zapata, G. Lahiner, B. Warot-Fonrose, J. Cure, Y. Chabal, A. Esteve and C. Rossi, *ACS Appl. Energy Mater.*, 2018, **1**, 1762–1770.
- 30 T. Wu, X. Wang, J. B. DeLisio, S. Holdren and M. R. Zachariah, *Carbon*, 2018, **130**, 410–415.
- 31 J. Pike, S.-W. Chan, F. Zhang, X. Wang and J. Hanson, *Applied Catalysis A: General*, 2006, **303**, 273–277.
- 32 P. E. Chen, N. C. Anderson, Z. M. Norman and J. S. Owen, *J. Am. Chem. Soc.*, 2017, **139**, 3227–3236.
- 33 Z. Bacsik and N. Hedin, *Vib. Spectrosc.*, 2016, **87**, 215–221.